

This is a repository copy of *Activation of Copper Species on Carbon Nitride for Enhanced Activity in the Arylation of Amines*.

White Rose Research Online URL for this paper:

<https://eprints.whiterose.ac.uk/165051/>

Version: Accepted Version

---

**Article:**

Vorobyeva, Evgeniya, Gerken, Viktoria C, Mitchell, Sharon et al. (15 more authors) (2020) Activation of Copper Species on Carbon Nitride for Enhanced Activity in the Arylation of Amines. ACS Catalysis. ISSN 2155-5435

<https://doi.org/10.1021/acscatal.0c03164>

---

**Reuse**

Items deposited in White Rose Research Online are protected by copyright, with all rights reserved unless indicated otherwise. They may be downloaded and/or printed for private study, or other acts as permitted by national copyright laws. The publisher or other rights holders may allow further reproduction and re-use of the full text version. This is indicated by the licence information on the White Rose Research Online record for the item.

**Takedown**

If you consider content in White Rose Research Online to be in breach of UK law, please notify us by emailing [eprints@whiterose.ac.uk](mailto:eprints@whiterose.ac.uk) including the URL of the record and the reason for the withdrawal request.

This document is confidential and is proprietary to the American Chemical Society and its authors. Do not copy or disclose without written permission. If you have received this item in error, notify the sender and delete all copies.

## Activation of Copper Species on Carbon Nitride for Enhanced Activity in the Arylation of Amines

Journal:	<i>ACS Catalysis</i>
Manuscript ID	cs-2020-03164r.R2
Manuscript Type:	Article
Date Submitted by the Author:	28-Aug-2020
Complete List of Authors:	<p>Vorobyeva, Evgeniya; Eidgenossische Technische Hochschule Zurich, Department for Chemistry and Applied Biosciences  Gerken, Viktoria; Eidgenossische Technische Hochschule Zurich, Department for Chemistry and Applied Biosciences  Mitchell, Sharon; Eidgenossische Technische Hochschule Zurich, Department for Chemistry and Applied Biosciences  Sabadell-Rendón, Albert; Institut Catala d'Investigacio Quimica  Hauert, Roland; Empa Materials Science and Technology, xi, shibo; Institute of Chemical and Engineering Sciences  Borgna, Armando; Institute of Chemical and Engineering Sciences, HC  Klose, Daniel; Eidgenossische Technische Hochschule Zurich, Laboratory of Physical Chemistry  Collins, Sean; University of Cambridge, Department of Materials Science and Metallurgy; University of Leeds  Midgley, Paul ; University of Cambridge, Department of Materials Science and Metallurgy  Kepaptsoglou, Demie; SFTC Daresbury Laboratory; University of York, Department of Physics  Ramasse, Quentin; SFTC Daresbury Laboratory; University of Leeds  Ruiz-Ferrando, Andrea; Institut Catala d'Investigacio Quimica  Fako, Edvin; Institut Catala d'Investigacio Quimica  Ortuño, Manuel; Institute of Chemical Research of Catalonia,  Lopez, Nuria; Universitat Rovira i Virgili Institut Catala d'Investigacio Quimica,  Carreira, Erick; Eidgenossische Technische Hochschule Zurich, Department for Chemistry and Applied Biosciences  Pérez-Ramírez, Javier; Eidgenossische Technische Hochschule Zurich, Institute for Chemical and Bioengineering</p>

SCHOLARONE™  
Manuscripts

# Activation of Copper Species on Carbon Nitride for Enhanced Activity in the Arylation of Amines

Evgeniya Vorobyeva,<sup>§,‡</sup> Viktoria C. Gerken,<sup>§,‡</sup> Sharon Mitchell,<sup>\*,§</sup> Albert Sabadell-Rendón,<sup>#</sup> Roland Hauert,<sup>¥</sup> Shibo Xi,<sup>†</sup> Armando Borgna,<sup>†</sup> Daniel Klose,<sup>§</sup> Sean M. Collins,<sup>±,∇</sup> Paul A. Midgley,<sup>±</sup> Demie M. Kepaptsoglou,<sup>±,||</sup> Quentin M. Ramasse,<sup>±,∇</sup> Andrea Ruiz-Ferrando,<sup>#</sup> Edwin Fako,<sup>#</sup> Manuel A. Ortuño,<sup>#</sup> Núria López,<sup>\*,#</sup> Erick M. Carreira,<sup>\*,§</sup> Javier Pérez-Ramírez<sup>\*,§</sup>

<sup>§</sup> Department of Chemistry and Applied Biosciences, ETH Zürich, Vladimir-Prelog-Weg 1-5, 8093 Zürich, Switzerland.

<sup>#</sup> Institute of Chemical Research of Catalonia and The Barcelona Institute of Science and Technology, 43007 Tarragona, Spain.

<sup>¥</sup> Empa, Swiss Federal Laboratories for Materials Science and Technology, Überlandstrasse 129, 8600 Dübendorf, Switzerland.

<sup>†</sup> Institute of Chemical and Engineering Sciences, A\*STAR, 1 Pesek Road, Jurong Island, Singapore 627833.

<sup>±</sup> Department of Materials Science and Metallurgy, University of Cambridge, Cambridge, CB3 0FS, U.K.

<sup>±</sup> SuperSTEM Laboratory, SciTech Daresbury Campus, Daresbury, WA4 4AD, U.K.

<sup>||</sup> Department of Physics, University of York, York, YO10 5DD, U.K.

<sup>∇</sup> School of Chemical and Process Engineering and School of Physics, University of Leeds, Leeds, LS2 9JT, U.K.

\* Corresponding authors. E-mails: msharon@chem.ethz.ch; nlopez@iciq.es; erickm.carreira@org.chem.ethz.ch; jpr@chem.ethz.ch.

‡ These authors contributed equally.

**Abstract**

We report the promoting effect of graphitic carbon nitride in Cu-catalyzed N-arylation. The abundance of pyridinic coordination sites in this host permits the adsorption of copper iodide from the reaction medium. The key to achieving high activity is to confine active Cu species on the surface, which is accomplished by introducing atomically-dispersed metal dopants to block diffusion into the bulk. The alternative route of incorporating metal during the synthesis of graphitic carbon nitride is ineffective as Cu is thermodynamically more stable in inactive subsurface positions. A combination of X-ray absorption, X-ray photoelectron, and electron paramagnetic resonance spectroscopy, density functional theory, and Kinetic Monte Carlo simulations is employed to determine the location and associated geometry as well as the electronic structure of metal centers. N-arylation activity correlates to the surface coverage by copper, which varies during the reaction due to an interplay between site formation via adsorption from the reaction medium and deactivation by diffusion into the bulk of the material, and is highest when an Fe dopant is used that hinders movement through the lattice.

**Key words:** Catalysts, Metals, Supports, C-N coupling, Copper, Carbon nitride, Catalyst deactivation.

## Introduction

Metal-mediated C-N bond formation via the cross-coupling of aryl halides with amines has been actively researched since its introduction in seminal works of Ullmann and Goldberg (Cu)<sup>1</sup> and more recently by independent works of Buchwald (Cu and Pd)<sup>2,3</sup> and Hartwig (Pd).<sup>4</sup> It now represents an indispensable tool for the construction of important fine-chemical and pharmaceutical intermediates.<sup>5-7</sup> Cu-mediated processes attract interest due to the continued pressure to move away from the use of precious metals, and there have been increasing efforts to improve their efficiency by increasing reaction rate, broadening substrate scope, or permitting operation under milder conditions.<sup>8,9</sup> In addition to Cu, Fe-catalyzed processes have also been explored to enable transformations under mild conditions,<sup>10</sup> and the combination of Fe and Cu as cooperative bimetallic catalytic systems has been reported to yield efficient performance.<sup>11-15</sup> However, these studies have also raised questions about the exact role of Fe,<sup>16</sup> and the mechanistic origin of potential synergistic effects with Cu remains unclear.

Several efforts have also been directed towards the development of N-arylation reactions mediated by heterogeneous copper catalysts, including copper nanoparticles supported on organic polymers,<sup>17,18</sup> bulk Cu-Fe hydrotalcite<sup>19</sup> and Cu-exchanged fluorapatite<sup>20</sup> phases, and immobilized Cu complexes<sup>21</sup>. Although attractive yields have been obtained, none of the systems have matched the specific activity of homogeneous catalysts. The decreased efficiency can arise from the intrinsically distinct electronic and geometric properties of active sites in metal nanoparticles compared to homogeneous complexes, or from the suboptimal organization, with many of the atoms inaccessible in the bulk of the metal-containing phases. Independent of the approach, evaluation of the heterogeneous catalysts in consecutive reaction cycles evidenced a progressive

1  
2  
3 decrease in the yield in all cases. Additionally, the nature of the active sites and the related  
4  
5 mechanism of N-arylation remain poorly understood.<sup>17-21</sup>  
6

7  
8 Single-atom heterogeneous catalysts (SAHCs) are promising alternatives to traditional systems for  
9  
10 replacement of their homogeneous counterparts, sharing structural similarities with those of  
11  
12 organometallic complexes.<sup>22-24</sup> To date, research targeting the use of these advanced catalysts for  
13  
14 this purpose has primarily focused on Rh-based SAHCs for hydroformylation<sup>25,26</sup> or Pd-based  
15  
16 SAHCs for Suzuki–Miyaura<sup>27</sup> or Ullmann-type<sup>28,29</sup> C-C coupling reactions. Graphitic carbon  
17  
18 nitride (GCN) is known to be able to stabilize single metal atoms in high concentration and was  
19  
20 recently shown to provide a flexible coordination environment for Pd atoms that could adapt to  
21  
22 the reaction requirements in Suzuki coupling.<sup>27</sup> Additionally, the crystalline structure of GCN  
23  
24 maximizes the uniformity of coordination sites for metal atoms, making these systems good  
25  
26 platforms for investigating the reactivity of distinct metal centers in other coupling reactions.  
27  
28  
29

30  
31 In this contribution, we prepare Cu-(Cu<sub>1</sub>/GCN), Fe- (Fe<sub>1</sub>/GCN) and Cu-Fe (Cu<sub>1</sub>Fe<sub>1</sub>/GCN) SAHCs  
32  
33 based on graphitic carbon nitride (GCN) to study their potential in Ullmann-type C–N bond-  
34  
35 forming reactions. However, none of the SAHCs are active when evaluated under state-of-the-art  
36  
37 conditions. Since GCN possesses abundant metal coordination sites, we evaluate the impact of  
38  
39 adding this material to the homogeneously-catalyzed reaction, which reveals a significant  
40  
41 promoting effect. The reaction rate is further enhanced by using Fe<sub>1</sub>/GCN. Detailed experimental  
42  
43 and computational analysis of the material provides insights on the interaction of the  
44  
45 heterogeneous component with CuI and the optimal coordination environment of supported copper  
46  
47 sites. Metal diffusion into the host is identified as a critical parameter determining reaction  
48  
49 kinetics. A descriptor for quantification of active species is developed using Kinetic Monte Carlo  
50  
51 simulations, by estimating surface coverage of Cu in the materials under the reaction conditions.  
52  
53  
54  
55  
56  
57  
58  
59  
60

## Experimental Section

**Catalyst Synthesis.** Metal-free GCN was prepared by calcination of dicyandiamide (Aldrich, >99%, 10 g) at 823 K (2.3 K min<sup>-1</sup> ramp rate) in a crucible for 4 h under a nitrogen flow (15 cm<sup>3</sup> min<sup>-1</sup>). Fe<sub>1</sub>/GCN, Cu<sub>1</sub>/GCN and Cu<sub>1</sub>Fe<sub>1</sub>/GCN were prepared via a one-pot synthesis. Dicyandiamide was ground for 15 min by hand in a mortar with Fe(NO<sub>3</sub>)<sub>3</sub>·9H<sub>2</sub>O (Sigma Aldrich, >98%), Cu(NO<sub>3</sub>)<sub>2</sub>·2.5H<sub>2</sub>O (Acros Organics (ACR), >98%), or both salts, respectively. The amount of salt added was calculated to achieve the desired metal content by considering a polymerization yield of GCN from dicyandiamide of 50%. Unlike cyanide compounds, dicyandiamide is stable under these conditions and widely used as a precursor for synthesis of carbon nitrides and N-doped carbons.<sup>30,31</sup> The resulting solid was placed in a tubular oven under N<sub>2</sub> flow (20 cm<sup>3</sup> min<sup>-1</sup>) and after flushing for 1 h at 373 K the mixture was heated up to 823 K (2.3 K min<sup>-1</sup> ramp rate) for 4 h. To investigate the effect of the atmosphere, the mixture of dicyandiamide and Fe(NO<sub>3</sub>)<sub>3</sub> (as described above) was placed in the static oven in air following the same heating procedure.

**Catalyst Characterization.** Inductively coupled plasma-optical emission spectrometry (ICP-OES) was conducted using a Horiba Ultra 2 instrument after dissolving the samples under sonication in a piranha solution. X-ray diffraction (XRD) was performed in a PANalytical X'Pert PRO-MPD diffractometer operated in Bragg-Brentano geometry using Ni filtered Cu K $\alpha$  ( $\lambda = 0.1541$  nm) radiation. Data were recorded in the range of 5-70° 2 $\theta$  (0.05° angular step size, 2 s per step). Thermogravimetric analysis was conducted in a Linseis PT1600 thermobalance in Ar (300 cm<sup>3</sup> STP min<sup>-1</sup>), heating the sample from 298-973 K (5 K min<sup>-1</sup> ramp). For microscopy analysis, the samples were dispersed as dry powders onto holey-carbon coated Cu or Ni grids. Scanning transmission electron microscopy (STEM) and energy dispersive X-ray spectroscopy (EDX) measurements were performed on a Talos F200X instrument (200 kV).

1  
2  
3 Aberration-corrected annular dark-field (AC-ADF) STEM imaging of Fe<sub>1</sub>/GCN and Fe<sub>1</sub>/GCN  
4 after 3 cycles was undertaken on a Hermes STEM (Nion, 60 kV, convergence semi-angle of  
5  
6 33 mrad) equipped with a cold field emission electron source and a Nion corrector for the probe-  
7  
8 forming optics, located at SuperSTEM, the U.K. National Research Facility for Advanced Electron  
9  
10 Microscopy. AC-ADF-STEM images of other samples were obtained using a Titan<sup>3</sup> 80-300  
11  
12 (ThermoFisher) microscope (300 kV, convergence semi-angle of 18 mrad) equipped with a high-  
13  
14 brightness 'X-FEG' electron source and a CEOS aberration corrector for the probe-forming optics.  
15  
16 In all cases, dwell time (<12 μs per pixel with beam currents <50 pA) and pixel size were  
17  
18 optimized to ensure sufficient signal-to-noise for single metal atom visibility while minimizing  
19  
20 beam-induced changes. X-ray photoelectron spectroscopy (XPS) was conducted in a Physical  
21  
22 Electronics Instruments Quantum 2000 spectrometer using monochromatic Al Kα radiation  
23  
24 generated from an electron beam operated at 15 kV and 32.3 W. The spectra were collected under  
25  
26 ultra-high vacuum conditions (5×10<sup>-7</sup> Pa) at a pass energy of 46.95 eV and referenced to the C 1s  
27  
28 peak of C<sub>3</sub>N<sub>4</sub> at 288.1 eV. X-ray absorption fine structure (XAFS) at the Cu and Fe K-edge were  
29  
30 acquired at the XAFCA beamline of the Singapore Synchrotron Light Source (SSLS, operated at  
31  
32 0.7 GeV with a maximum current of 200 mA).<sup>32</sup> The data were collected in transmission mode  
33  
34 using ion chamber detectors, except for the analysis of the Cu K-edge of the used catalysts, which  
35  
36 were collected in fluorescence mode using a silicon drift detector. All samples were pelletized as  
37  
38 disks (10 mm diameter, 1 mm thick) using boron nitride as a binder. The XAFS data were  
39  
40 processed using the ATHENA module in the Demeter packages following standard procedures.<sup>33</sup>  
41  
42 Quantitative structural parameters were obtained using the ARTEMIS module via a least-squares  
43  
44 curve parameter fitting method (**Table S1**).<sup>33</sup> Very similar results were also obtained using  
45  
46 LARCH (**Table S2**).<sup>34</sup> Continuous-wave electron paramagnetic resonance (cw-EPR) spectra of  
47  
48  
49  
50  
51  
52  
53  
54  
55  
56  
57  
58  
59  
60



1  
2  
3 powder samples in quartz tubes (3 mm OD, 1 cm filling height) were recorded at a microwave  
4 frequency of approximately 9.5 GHz on an Elexsys E580 EPR spectrometer (Bruker Biospin)  
5 equipped with a cylindrical resonator and an ESR900 helium flow cryostat (Oxford Instruments)  
6 to stabilize the temperature to 5 K. Cw-EPR spectra were recorded under non-saturating conditions  
7 at a microwave power of 0.2 mW, unless stated. For detection a magnetic field modulation of  
8 0.2 mT and 100 kHz was applied and the modulated signal was amplified by a lock-in amplifier  
9 (81.92 ms conversion time, 40.96 ms time constant), sweeping the magnetic field from 2.5-  
10 1000 mT in 4096 steps. The magnetic field offset was corrected using DPPH (Sigma Aldrich) as  
11 a reference and the spectrometer baseline was subtracted using an empty quartz capillary as a  
12 reference.  
13  
14  
15  
16  
17  
18  
19  
20  
21  
22  
23  
24  
25

26 **Catalyst Evaluation.** A vial containing a magnetic stirring bar was charged with Fe<sub>1</sub>/GCN  
27 (1 mol%), CuI (5 mol%), amine (1 equiv.; if solid), aryl iodide (1 equiv.; if solid) and Cs<sub>2</sub>CO<sub>3</sub>  
28 (2 equiv.). Dry dimethyl formamide (DMF, 0.9 cm<sup>3</sup>) was added, along with aryl iodide (1 equiv.;  
29 if liquid) and amine (1 equiv.; if liquid). The vials were flushed with argon, sealed with urethane  
30 screw caps with PTFE inserts, and heated to 393 K for 12 h. After cooling to room temperature,  
31 the reaction mixture was diluted with DCM (1 cm<sup>3</sup>) and filtered either through a syringe filter or  
32 through a Büchner funnel, lined with filter paper. The residue was washed with DCM (2 × 2 cm<sup>3</sup>)  
33 and water (2 × 3 cm<sup>3</sup>). The phases of the filtrate were separated and the aqueous phase was washed  
34 with DCM (3 × 5 cm<sup>3</sup>). The combined organic layers were washed with brine and dried over  
35 MgSO<sub>4</sub>. The solvent was removed under reduced pressure and the crude product was purified by  
36 silica gel chromatography with an eluent of hexane and ethyl acetate. Complete details of the  
37 procedures for catalytic testing are provided in **Note S1**.  
38  
39  
40  
41  
42  
43  
44  
45  
46  
47  
48  
49  
50  
51  
52  
53  
54  
55  
56  
57  
58  
59  
60

1  
2  
3 **Computational Details.** Spin unrestricted density functional theory (DFT) simulations were  
4 performed using the Vienna Ab Initio Simulation Package code<sup>34,35</sup> to gain further understanding  
5 of the metal-scaffold interactions and the cooperative effect of Cu and Fe in the N-arylation  
6 reaction. A generalized gradient approximation was employed, expressed by the Perdew–Burke–  
7 Ernzenhof functional<sup>36</sup> with the D3 correction<sup>37</sup> to describe van der Waals interactions. Inner  
8 electrons were represented as projector augmented wave potentials<sup>38,39</sup> and the valence electrons  
9 were expanded in plane waves with a cut-off kinetic energy of 450 eV. Models for the GCN,  
10 Fe<sub>1</sub>/GCN and Cu<sub>1</sub>/GCN samples were constructed as well as for potential structures formed in situ  
11 (in the presence of CuI, totaling to ca. 200 structures) in a (2 × 2) heptazinic supercell with four  
12 layers. Our approach implies that to maintain electroneutrality, the charge of the adsorbed atoms  
13 is redistributed effectively in the  $\pi$ -system of the host. This is clearly seen in **Figure S1**, where the  
14 density of the Cu<sub>1</sub>/GCN is subtracted from that of the carbon matrix and Cu itself. It becomes clear  
15 that while the Cu gets positively charged the missing charge is redistributed in the  $\pi$ -system of  
16 GCN. Multireference configurations cannot be introduced easily by DFT but, due to the lack of  
17 strong interaction in the dimers, these effects are minor compared to those associated with the  
18 liquid-solid material exchange. Consistent with the limited interaction between the cations, the  
19 shortest identified Cu–Fe distance is 2.60 Å. As the reaction consists of two phases and Cu can be  
20 present either in solution or in the material, it is crucial to determine the amount and location (i.e.  
21 surface or bulk) of metal in GCN by taking into account concentration effects over time and  
22 extending the spatial dimension. To this end, Kinetic Monte Carlo (KMC) simulations<sup>40</sup> were  
23 performed. This allows us to introduce time as a variable and the liquid as a reservoir for the  
24 material, thereby permitting the dynamic study of the system. Unlike other kinetic procedures such  
25 as microkinetics, it also preserves the spatial dependence between the different cavities. The KMC  
26  
27  
28  
29  
30  
31  
32  
33  
34  
35  
36  
37  
38  
39  
40  
41  
42  
43  
44  
45  
46  
47  
48  
49  
50  
51  
52  
53  
54  
55  
56  
57  
58  
59  
60

1  
2  
3 runs were done by adapting our in-house code with a ( $100 \times 100$ ) surface cell and 10 layers of the  
4 simulation cell. The diffusion (percolation through the nanoporous heptazinic holes) and  
5 dimerization (formation of metal–metal bonds) paths were sampled at the DFT level and the  
6 thermodynamic and kinetic parameters obtained were employed as input in the KMC together with  
7 the experimental temperature and stoichiometry. Benchmarks for larger KMC runs and error  
8 estimations are found in **Tables S3** and **S4** and **Figures S2** and **S3**. Extended computational details  
9 are provided in **Note S2**. All computed structures can be found online and are freely available  
10 through the ioChem-BD database.<sup>41,42</sup>  
11  
12  
13  
14  
15  
16  
17  
18  
19  
20  
21  
22  
23

## 24 **Results and Discussion**

25  
26 **Single-atom heterogeneous catalysts.** To evaluate the potential of SAHCs for the arylation of  
27 amines, three metal-doped graphitic carbon nitride (GCN) systems containing Cu (denoted  
28  $\text{Cu}_1/\text{GCN}$ ), Fe ( $\text{Fe}_1/\text{GCN}$ ), or both metals ( $\text{Cu}_1\text{Fe}_1/\text{GCN}$ ) were prepared by introducing the  
29 corresponding nitrate salts during the polymerization of dicyandiamide (**Figure 1a**). The  
30 importance of ensuring inert conditions during the synthesis was shown by conducting the same  
31 treatment in air, which resulted in the formation of a bulk  $\text{Fe}_x\text{O}_y$  phase with low carbon content  
32 (**Figure S4**).

33  
34 Careful examination by aberration-corrected annular dark-field scanning transmission electron  
35 microscopy (AC-ADF)STEM demonstrated the predominant presence of isolated metal atoms in  
36 all samples (**Figure 1b-d** and **Figure S5**). Small metal clusters (<1 nm) were detected in  
37  $\text{Cu}_1\text{Fe}_1/\text{GCN}$ , but only in a few of the large number of locations studied. The high density of atoms  
38 in these catalysts makes it difficult to exclude the presence of small metal ensembles such as dimers  
39 and trimers from simple inspection of the images. Note that AC-ADF-STEM images were acquired  
40  
41  
42  
43  
44  
45  
46  
47  
48  
49  
50  
51  
52  
53  
54  
55  
56  
57  
58  
59  
60

1  
2  
3 with an electron exposure to identify single atoms while minimizing beam-induced motion,  
4 resulting in relatively high noise levels. Statistical analysis of the nearest-neighbor distances  
5 (NND) supported the predominance of single atoms, the observed distribution closely matching  
6 that theoretically expected for a random arrangement.<sup>43</sup> The high dispersion of the desired metals  
7 was also confirmed by STEM imaging coupled with energy-dispersive X-ray (EDX) spectroscopy  
8 at lower magnification (**Figures 1b-d** and **S6**). Consistently, no metal-metal bonds were detected  
9 in the Fourier transformed extended X-ray absorption fine structure (FT-EXAFS) spectra of any  
10 of the samples (**Figure 2a,b**). Dominant contributions around 1.6 Å for Cu and 1.8 Å for Fe,  
11 correspond to the expected positions of the metals bound to nitrogen in the structure. Note that,  
12 although it is not possible to discriminate Cu–N from Cu–O or Cu–C bonds only from FT-EXAFS  
13 spectrum, coordination with nitrogen in the GCN scaffold would be thermodynamically preferred  
14 over carbon and the catalysts were prepared under inert conditions. Derivation of the coordination  
15 number (CN) based on fitting of the EXAFS data gives a value of 3.1 for Cu and 4.8 for Fe  
16 (**Table S1**).

17  
18  
19  
20  
21  
22  
23  
24  
25  
26  
27  
28  
29  
30  
31  
32  
33  
34  
35  
36  
37  
38  
39  
40  
41  
42  
43  
44  
45  
46  
47  
48  
49  
50  
51  
52  
53  
54  
55  
56  
57  
58  
59  
60  
Density functional theory simulations reveal that both Cu and Fe are likely stabilized as isolated  
centers in two generally preferred locations within the GCN lattice (**Figure 3a**). These correspond  
to the interlayer “i” and the subsurface heptazinic “u” positions, with a difference in simulated  
core-level shifts of 1.3 eV (**Table S5**). To quantify the relative stability, formation energies were  
computed using an empty cavity and an isolated atom as reference states (**Table S6**). For both  
metals, the interlayer motif “i” (**Figure 3b**) is more stable than the subsurface “u” (surface “s”) by  
0.74 eV (1.03 eV) for Fe and 0.54 eV (0.59 eV) for Cu. Consistent with the experimental results,  
homo- or heteronuclear dimers or trimers of Cu and Fe were found to be generally less stable than  
isolated atoms in the same coordination sites (**Table S7**), and therefore unlikely to form

1  
2  
3 (endothermic in the range from 0.64 to 3.85 eV referenced to isolated atoms in the “i” positions,  
4 **Table S8**). In fact, the displacement of metal atoms from the “i” motif to any other position  
5  
6 available in the material (of the large set of explored structures ~200, **Table S9**) was found to be  
7  
8 endothermic.  
9  
10

11  
12 Comparison of the XANES spectra evidences a valence state of between +1 and +2 for Cu based  
13  
14 on comparison with reference samples (**Figure S7**). This is consistent with previously reported  
15  
16 values for Cu SAHCs.<sup>44-46</sup> It is not possible to assign the Cu oxidation state from the Cu 2p XPS  
17  
18 spectrum alone due to the identical binding energies of Cu<sup>0</sup> and Cu<sup>+</sup>, but the absence of shake up  
19  
20 excitations around 940-944 eV indicates that no significant amount of Cu<sup>2+</sup> is present at the surface  
21  
22 (**Figure 2c**). Examination of the corresponding Cu LMM Auger spectra (**Figure 2e**), which  
23  
24 exhibits a prominent peak at 571.2 eV, points to the presence of Cu<sup>+</sup>, consistent with the expected  
25  
26 cationic nature of isolated metal centers in GCN.<sup>47</sup> The shape of the Auger signal points to Cu<sub>2</sub>O  
27  
28 with no metallic Cu present, which is usually the expected surface compound for air exposed Cu.  
29  
30  
31 However, the Auger peak does not appear at the exact reference position for bulk Cu<sub>2</sub>O which is  
32  
33 569.7 eV,<sup>48</sup> but is shifted to 571.6 eV binding energy. This shift has been described before to occur  
34  
35 when Cu<sub>2</sub>O is dispersed in submonolayer form.<sup>49</sup> In the EPR spectra (**Figure 2f**), the characteristic  
36  
37 hyperfine quartet structure, consisting of three resolved, equally spaced peaks at 280, 301, and  
38  
39 322 mT, provides evidence for the presence of Cu<sup>2+</sup> due to its nuclear spin of  $I = 3/2$ . The fact that  
40  
41 Cu<sup>2+</sup> species are not observed by XPS indicates that they likely originate from Cu in the bulk of  
42  
43 the material. Identifying the correct fingerprints to analyze the speciation of metal atoms on carbon  
44  
45 materials theoretically is highly nontrivial, and care must be taken to ensure that charges are  
46  
47 adequately considered.<sup>50,51</sup> Adsorption in the cavities of GCN provide species with M<sup>δ+</sup> character,  
48  
49 where the host accommodates the extra charge, while inside the lattice the metal centers are more  
50  
51  
52  
53  
54  
55  
56  
57  
58  
59  
60

1  
2  
3 positively charged. In agreement with the experimental data, both Cu species are positively  
4 charged with a difference in simulated core-level shifts of 0.9 eV between the “i” and “u” positions.  
5  
6 Determination of the chemical state of Fe by XPS requires caution due to the multiple possible  
7 species with overlapping binding energies.<sup>52</sup> Careful analysis of the Fe 2*p* XPS spectrum identifies  
8 the presence of two oxidized species, with the majority attributed to Fe<sup>2+</sup> and a slightly lower  
9 amount of Fe<sup>3+</sup> (**Figure 2e**). Consistently, EPR measurements evidence a signal with a *g*-value of  
10 4.3 that corresponds to Fe<sup>3+</sup> (**Figure 2f**). Additional transitions near zero magnetic field in the X  
11 band could potentially originate from high spin Fe<sup>2+</sup> species with axial coordination, as has been  
12 theoretically demonstrated.<sup>53</sup> Finally, the characterization of the Cu and Fe centers in Cu<sub>1</sub>Fe<sub>1</sub>/GCN  
13 reveals that the properties are virtually equivalent to those evidenced for samples containing only  
14 a single metal. In all cases, a lower metal content is detected on the catalyst surface with respect  
15 to the bulk (**Table 1**), which agrees with the uniform distribution throughout the GCN host as  
16 expected using a direct polymerization approach for metal introduction.<sup>47</sup> Analysis of the  
17 composition of the near-surface region (ca. 0.5-2 nm depth) by XPS confirms the low oxygen  
18 content, which does not exceed 2 atomic percent (at%) in any of the samples.

19  
20 The catalytic performance of Fe<sub>1</sub>/GCN, Cu<sub>1</sub>/GCN, and Cu<sub>1</sub>Fe<sub>1</sub>/GCN was investigated in the  
21 arylation of *N*-heterocycles (**Figure 4a**). Different variables such as the source and amount of  
22 metal, the base, solvent, temperature, and the type of aryl halide influence this reaction, and the  
23 initial choice was based on the best-reported results.<sup>5</sup> Specifically, the reactions were carried out  
24 with 5 mol% of the copper source, 1 mol% of the iron source, and 2 equiv. Cs<sub>2</sub>CO<sub>3</sub> in DMF at  
25 393 K. As a point of reference, the Ullman coupling reaction of iodobenzene (**1a**) and pyrazole  
26 (**2a**) is catalyzed by CuI in the absence of Fe, producing 1-phenyl-1*H*-pyrazole (**3a**) in 44% yield  
27 after 6 h. When the reaction is conducted with CuI in combination with FeCl<sub>3</sub> for 6 h, only slight  
28  
29  
30  
31  
32  
33  
34  
35  
36  
37  
38  
39  
40  
41  
42  
43  
44  
45  
46  
47  
48  
49  
50  
51  
52  
53  
54  
55  
56  
57  
58  
59  
60

1  
2  
3 increase in yield (50%) is observed. In comparison, experiments revealed that neither of the  
4  
5 Cu-containing SAHCs ( $\text{Cu}_1/\text{GCN}$  or  $\text{Fe}_1\text{Cu}_1/\text{GCN}$ ) catalyzes the reaction when replacing CuI  
6  
7 under equivalent conditions.  
8  
9

10 **Enhanced efficiency through surface activation.** Solid surfaces also attract interest as promoters  
11  
12 in coupling reactions through surface-confinement.<sup>54</sup> Considering the abundance of metal  
13  
14 coordination sites in the host, we examined the influence of adding GCN (50 wt% relative to  
15  
16 pyrazole) to the CuI-catalyzed reaction (**Figure 4b**). Interestingly, a considerably enhanced yield  
17  
18 of **3a** (70%) was observed after 6 h. A similar effect was observed if GCN was substituted with  
19  
20  $\text{Cu}_1/\text{GCN}$ , but surprisingly the introduction of  $\text{Fe}_1/\text{GCN}$  led to a remarkable further enhancement  
21  
22 leading to 1-phenyl-1*H*-pyrazole in quantitative yield after only 4 h. Based on the total Cu content,  
23  
24 this results in a five-fold increase in the turnover frequency (TOF) compared to the standard  
25  
26 CuI-catalyzed reaction (**Figure 4b**), while GCN alone leads to almost a 2-fold increase. Since  
27  
28  $\text{Fe}_1/\text{GCN}$  and GCN exhibit virtually equivalent surface area, this suggests that presence of Fe in  
29  
30 the lattice plays an important role. Unfortunately, quantitative comparison with TOFs reported in  
31  
32 literature is not possible since previous studies on homogeneous versions of this reaction did not  
33  
34 report sufficient data to calculate them,<sup>55</sup> and values may vary widely for other substrates.  
35  
36  
37

38  
39 The systematic evaluation of copper catalysts in N-arylation reactions is essential because of well-  
40  
41 known reproducibility issues related to the variable induction periods resulting from the use of  
42  
43 partially soluble inorganic bases<sup>56</sup> and the possible presence of metal contaminants.<sup>16</sup> Our study  
44  
45 shows that the carbon nitride promotes the state-of-the-art homogeneous copper catalyst ( $\text{CuI}$ )<sup>5</sup>,  
46  
47 leading to higher turnover frequency when benchmarked against known methods under  
48  
49 comparable reaction conditions. A wide array of parameters including the temperature and time  
50  
51 (**Table S10**), copper source (**Table S11**), and the choice of base and other additives (**Table S12**)  
52  
53  
54  
55  
56  
57  
58  
59  
60

1  
2  
3 were evaluated to identify the maximal promotional effect upon addition of Fe<sub>1</sub>/GCN. It was found  
4 that both Cu<sup>+</sup> and Cu<sup>2+</sup> could be employed as Cu sources. The presence of copper salts (such as  
5 triflates, sulfates, or halides) is crucial for the reaction and cannot be replaced by salts of other  
6 metals. In contrast, the nature of the ligand appears less influential. The addition of Cs<sub>2</sub>CO<sub>3</sub> is  
7 essential, and omitting it or replacing it with K<sub>2</sub>CO<sub>3</sub> gave no product formation (0%). Replacement  
8 of GCN with an activated carbon host reduced the efficiency of the arylation reaction, producing  
9 only a yield of less than 20% (**Figure S8**). This suggests that the abundant pyridinic sites in  
10 graphitic carbon nitride play an important role in enhancing the kinetics of N-arylation. The  
11 structure differs from that of previously reported copper complexes with dicyandiamide as a  
12 ligand, as this molecule binds the metal via a nitrile nitrogen.<sup>57</sup> The latter creates a similar  
13 coordination environment to that generated when acetonitrile is used as a solvent, which doesn't  
14 enhance the reaction kinetics compared to the use of DMF.

15  
16  
17 To study the effect of the Fe content in Fe<sub>1</sub>/GCN, three distinct samples were prepared (**Figure S4**).  
18  
19 Analysis by XRD revealed a loss of the crystalline order of the host at very high metal loading  
20 (20 wt%), which led to reduced stability of the metal atoms and formation of nanoparticles.  
21  
22 However, variation of the Fe content between 0.4–5.4 wt% did not alter speciation, but led to a  
23 proportional increase in surface metal concentration as determined by XPS (**Figure S9, Table 1**).  
24  
25 Evaluation of the resulting materials using an equivalent Fe amount revealed a similar  
26 enhancement of the yield of 1-phenyl-1*H*-pyrazole (**3a**) over all Fe-doped samples, which indicates  
27 that the structure of the active center was equivalent in all cases (**Figure S8**).

28  
29 To gain insight into the promotional effect of Fe<sub>1</sub>/GCN, we evaluated its reusability in consecutive  
30 catalytic runs. To investigate the potential activity of adsorbed species, the catalytic solid was  
31 isolated and washed after 12 h in the reaction medium and the recovered material was tested in a  
32  
33  
34  
35  
36  
37  
38  
39  
40  
41  
42  
43  
44  
45  
46  
47  
48  
49  
50  
51  
52  
53  
54  
55  
56  
57  
58  
59  
60



1  
2  
3 freshly prepared reaction mixture containing no CuI. However, no coupling products were  
4  
5 observed, indicating that the active species are not preserved in the used catalyst. In contrast, if  
6  
7 CuI was freshly added in each run, the used heterogeneous Fe<sub>1</sub>/GCN component achieved  
8  
9 quantitative yields in five consecutive 12 h runs. To understand the interaction of CuI with the  
10  
11 Fe<sub>1</sub>/GCN promoter and associated structural impact, the isolated and dried Fe<sub>1</sub>/GCN sample was  
12  
13 characterized following each run. Low magnification STEM images of the used sample confirm  
14  
15 the absence of metal nanoparticles and elemental maps indicate that copper is incorporated on the  
16  
17 surface of the GCN particles (**Figure 5a,b**). AC-ADF-STEM images evidence a high density of  
18  
19 atomically-dispersed metal species (**Figure S10**). The presence of iron in these areas was  
20  
21 confirmed by electron energy loss spectroscopy at the Fe *L*<sub>23</sub> edge (**Figure 5c**), which also  
22  
23 identified the presence of cesium species originating from the Cs<sub>2</sub>CO<sub>3</sub> base applied in the reaction.  
24  
25 Chemical analyses confirm that the Fe content remains constant, pointing to the absence of Fe  
26  
27 leaching, and provides evidence for the accumulation of appreciable amounts of Cu (ca. 10% of  
28  
29 the Cu present in solution) that must also be present as single atoms (**Table 1**). The amount of  
30  
31 copper incorporated reaches a maximum after three runs, which could indicate the development of  
32  
33 an equilibrium between the copper present in the reaction medium and adsorbed on the solid. To  
34  
35 investigate the possibility of saturating the sample with copper to avoid deactivation of the active  
36  
37 species by diffusion into the bulk (*vide infra*), the sample recovered after five consecutive runs  
38  
39 was tested without adding CuI, but the yields remained negligible. Reducing the amount of CuI  
40  
41 applied to promote full uptake from the reaction medium or increasing the concentration to  
42  
43 promote higher uptakes did not prove straightforward, due to slow kinetics or poor solubility,  
44  
45 respectively. No iodine was detected in the used samples by EDX, indicating that the function of  
46  
47 the GCN is not simply as a base to remove the HI produced during the reaction.  
48  
49  
50  
51  
52  
53  
54  
55  
56  
57  
58  
59  
60

1  
2  
3 Inspection of FT-EXAFS spectra of used Fe<sub>1</sub>/GCN at the Cu K-edge shows that the coordination  
4 sphere of Cu deposited on the catalyst surface during the reaction is altered when compared to that  
5 observed for CuI: A Cu–N(O) bond at 1.5 Å strongly suggests coordination with the GCN scaffold  
6  
7  
8 (Figure 5d). The CNs of Cu atoms are similar to those observed from Cu<sub>1</sub>/GCN and Cu<sub>1</sub>Fe<sub>1</sub>/GCN  
9  
10 (Table S1). Analysis of the Fe K-edge indicates that the coordination environment of Fe sites is  
11  
12 largely unaffected by the adsorption of other metals (Figure 5e, Table S1). Comparison of  
13  
14 XANES spectra at the respective edges of both metals (Figure S7), shows that the Cu species  
15  
16 incorporated during the reaction are slightly more oxidized than when the metal is introduced  
17  
18 during the synthesis, providing evidence for edge positions closer to that of the CuO than the Cu<sub>2</sub>O  
19  
20 reference (Figure 5f). This is consistent with the higher XPS shift computed for CuI in surface  
21  
22 sites (0.27 eV) than for Cu in the same position (–0.01 eV) or in subsurface (–0.90 eV) sites  
23  
24 (Table S2). In contrast, Fe centers shift to slightly lower positions after use of Fe<sub>1</sub>/GCN in the  
25  
26 reaction. XPS data show that the surface concentration of Cu increases to much higher values than  
27  
28 the surface metal contents of any of the as-synthesized SAHCs (Table 1), and analysis of the  
29  
30 Auger spectra confirms the presence of Cu<sup>+</sup> species at the surface. In contrast, the surface Fe  
31  
32 content drops to almost zero after the first run, which suggests that it is not directly involved in the  
33  
34 catalytic cycle, and agrees with the absence of Fe leaching. In agreement with the findings of  
35  
36 XAFS, XPS data provides evidence for a lower degree of oxidation, with a decreased proportion  
37  
38 of Fe<sup>3+</sup> with respect to Fe<sup>2+</sup>. EPR analyses confirm the presence of isolated Cu<sup>2+</sup> species, but the  
39  
40 signals are broader and shift to lower magnetic fields compared to the fresh Cu<sub>1</sub>/GCN or  
41  
42 Cu<sub>1</sub>Fe<sub>1</sub>/GCN, suggesting a less well-defined coordination sphere (Figure 5g). Slight variations in  
43  
44 intensities of EPR spectra can originate from differences in sample conductivity (Figure S11).  
45  
46  
47  
48  
49  
50  
51  
52  
53  
54  
55  
56  
57  
58  
59  
60

1  
2  
3 Having identified optimal reaction conditions, additional partners in the N-arylation reaction were  
4 examined (**Figure 6**). Aryl iodides bearing electron-donating (**3c**) and electron-withdrawing  
5 substituents (**3d-3g**) furnished products in quantitative yields. Notably, compounds containing an  
6 aryl chloride (**3f**) or aryl bromide (**3g**) could be employed with the coupling reaction displaying  
7 high degree of chemoselectivity for iodide. The remaining halides in the products enable further  
8 functionalization by implementation of numerous other coupling reactions. The reaction also  
9 works with substrates incorporating reactive sites with adjacent methyl groups (**3b**). Moreover,  
10 iodo-heteroarenes (**3i** and **3j**) are good substrates for the reaction. In contrast, variation of the  
11 amine nucleophile had a more profound influence on the outcome of the reaction. Introducing  
12 methyl groups on the pyrazole reduces the yield significantly to 71% (**3k**) and 53% (**3l**). Other  
13 heterocyclic amines could also be used as coupling partners (**3m-3p**), as well as functionalized  
14 *N*-heterocycles bearing a free alcohol (**3q**) or an ester (**3r**).

15  
16  
17  
18  
19  
20  
21  
22  
23  
24  
25  
26  
27  
28  
29  
30  
31 ***In situ* formation of the active species.** The mechanism of CuI-catalyzed reaction in  
32 homogeneous phase has been both experimentally<sup>58</sup> and computationally<sup>59-61</sup> studied in the  
33 literature. Our study has shown that a two-fold enhancement in activity can be achieved by  
34 introducing metal-free GCN material and that nearly quantitative yields can be obtained after 4 h  
35 through doping the lattice of GCN with Fe single atoms. To rationalize this remarkable  
36 promotional effect, the synergy between the solution reservoir of CuI molecules and the Fe atoms  
37 dispersed in GCN to form the active species needs to be considered in the simulations. As the  
38 formation of metal ensembles in which Fe atoms could directly affect the Cu sites within the  
39 material appears energetically uncompetitive, the interactions between CuI and GCN or the Fe- or  
40 Cu-doped analogs were evaluated by DFT.

1  
2  
3 After extensive sampling of the possible coordination geometries over the support (**Figure S12**),  
4 CuI was found to adsorb and reside on the surface heptazine cavity of GCN. Due to the bulky  
5 nature of the anion and the relatively strong Cu–I bond, both the penetration of this molecule into  
6 the lattice and dissociation are strongly endothermic (>2 eV). When Fe is sitting in the subsurface  
7 interlayer “i” (the most stable position) and CuI is adsorbed in the same heptazine cavity, no  
8 electronic perturbation to the Cu–I bond (or change in the Bader charge) is observed, suggesting  
9 that Fe does not have a co-catalytic role. This is because configurations in which Fe–Cu bonds are  
10 formed have lower stability in comparison to ensembles that occupy the same cavity, the distances  
11 are relatively large (2.60 Å), indicative of a weak bond (the neutral dimer distance is 2.31 Å,  
12 BE = 1.56), this is due to the fact that both species are positively charged.<sup>62</sup> Therefore, the active  
13 sites comprise Cu atoms partially coordinated on the surface of the macroheterocycle (either as Cu  
14 or as the Cu–I that would need a preactivation step), but Fe does not appear to have a direct  
15 electronic effect on the reaction mechanism.  
16  
17  
18  
19  
20  
21  
22  
23  
24  
25  
26  
27  
28  
29  
30  
31  
32

33 The fact that the coordination of CuI to heptazine sites in GCN can generate a more active species  
34 than the purely homogeneous CuI seems reasonable considering that diamine,<sup>55,63,64</sup> pyridine,<sup>65,66</sup>  
35 and phenanthroline<sup>67,68</sup> based ligands have previously been shown to promote CuI-catalyzed  
36 N-arylation reactions.<sup>5,69</sup> In our systems the carbon scaffold can be seen as acting as the ligand.  
37 Calculations of initial stages of the interaction of pyrazole and iodobenzene with the CuI-Fe<sub>1</sub>/GCN  
38 system indicate that there is no energy improvement with respect to the CuI-catalyzed reaction in  
39 solution (**Table S13**, the adsorption energy of reactants differs by only 0.1 eV). However,  
40 differences can be anticipated in other terms, in particular in surface confinement and the potential  
41 interaction with the GCN lattice would lead to elevated concentration of substrates at the interface.  
42 In addition, translational entropy contributions will favor the confined system.  
43  
44  
45  
46  
47  
48  
49  
50  
51  
52  
53  
54  
55  
56  
57  
58  
59  
60

1  
2  
3 **Accumulation of the active species.** Static DFT cannot account for the highly dynamic nature of  
4 the system where a close interrelationship between solution and material is crucial to understand  
5 the reactivity and dominates other potential electronic terms. The reaction medium surrounding  
6 the GCN material acts as a CuI reservoir, and active metal species, either initially present in the  
7 GCN lattice or incorporated from the solution, can deactivate by diffusion into the bulk of the  
8 material. To account for concentration effects over time we employed Kinetic Monte Carlo (KMC)  
9 simulations, mimicking metal content and distribution of experimentally synthesized samples.  
10 KMC is needed to include simultaneously the time dependences and the geometric constraints and  
11 links that would be lost in a mean-field approach. In particular, we considered Fe<sub>1</sub>/GCN containing  
12 5.6, 4.1, or 0.4 wt% of Fe, Cu<sub>1</sub>/GCN containing 1.7 wt% of Cu, and metal-free GCN at 393 K. As  
13 a starting point, the stoichiometric metal loading was randomly distributed over the 100 × 100 × 10  
14 coordination positions considered in the simulation. These sites were connected according to the  
15 structure of GCN (**Figure S13**). When Fe<sub>1</sub>/GCN or Cu<sub>1</sub>/GCN systems are considered as isolated  
16 systems (i.e. no CuI reservoir), the coverage of surface metal atoms decays in a very short time.  
17 The metal atoms percolate from the surface to inner positions within the material, and finally only  
18 “i” positions remain populated (**Figure S14**). The absence of surface metal species explains the  
19 inactivity of the Cu- and Fe-SAHCs as heterogeneous catalysts.  
20  
21  
22  
23  
24  
25  
26  
27  
28  
29  
30  
31  
32  
33  
34  
35  
36  
37  
38  
39  
40  
41

42 Extending the simulations to account for the presence of CuI, high coverage of isolated Cu atoms  
43 were introduced in “s” positions (assuming that Cu atoms originate from CuI followed by the  
44 removal of I during the coupling reaction, **Figure 7a**). For GCN, evolving the system to estimate  
45 the deactivation of active species via percolation resulted in a homogeneous distribution of Cu  
46 atoms in “i” positions (**Figure 7b**). Interestingly, when starting from the equilibrated Fe<sub>1</sub>/GCN,  
47 the percolation of the Cu in “s” is reduced with increasing Fe concentration (**Figure S15**). For  
48  
49  
50  
51  
52  
53  
54  
55  
56  
57  
58  
59  
60

1  
2  
3 example, the average time to completely deplete the surface Cu in 0.4Fe<sub>1</sub>/GCN or Cu<sub>1</sub>/GCN is  
4  
5  $(3.0 \pm 0.1) \times 10^{-5}$  s and  $(2.5 \pm 1.9) \times 10^{-4}$  s, respectively.  
6  
7

8 Assuming that the activity of a catalyst relates to its ability to maintain a higher concentration of  
9  
10 active copper sites at surface “s” positions, we evaluated the coverage-time curves ( $\theta_{\text{Cu-s}}(t)$ ,  
11  
12 **Figure 7c**) for different supports. The integral of  $\theta_{\text{Cu-s}}(t)$  (denoted as  $\Theta_{\text{Cu-s}}$ ) represents the total  
13  
14 number of active sites and thus the ability of the catalyst to inhibit percolation (further details are  
15  
16 presented in **Note S2**, **Table S14**, and **Figures S15**, **S16**, and **S17**). Comparison of the product  
17  
18 yields as a function of  $\Theta_{\text{Cu-s}}$  (**Figure 7d**) reveals a strong correlation consistent with the *in situ*  
19  
20 formation and deactivation of the active species on the surface of GCN. This dynamic behavior  
21  
22 can be intuitively understood by considering the symmetry of GCN, where interlayer positions “i”  
23  
24 represent knots in the KMC grid (**Figure S13**). GCN and Cu<sub>1</sub>/GCN show converging behaviors  
25  
26 due to the identical mobility of Cu that is introduced in the catalytic cycle to that present in the as-  
27  
28 prepared catalyst. Namely, the initial Cu coverage gradient drives the mobility of Cu in the “i”  
29  
30 positions reducing their blocking effect and causing percolation. However, the presence of the  
31  
32 more stable Fe atoms in “i” positions triggers a cascade effect, where a single localized Fe atom  
33  
34 blocks a whole branch of Cu diffusion trajectories. Consequently, a clustering of yields and  $\Theta_{\text{Cu-s}}$   
35  
36 is observed.  
37  
38  
39  
40  
41

42 The location of metal atoms in SAHCs, and especially those based on nanoporous hosts, remains  
43  
44 poorly understood and challenging to characterize. Our findings show that the diffusion of metal  
45  
46 species into energetically favorable positions within the bulk of carbon nitride is a primary  
47  
48 mechanism of deactivation (**Figure 7a**). One strategy to preserve high concentrations of active  
49  
50 species on the surface is to block their percolation into subsurface positions. In GCN, this can be  
51  
52 achieved by doping the lattice with inactive metal atoms. KMC simulations of the behavior of  
53  
54  
55  
56  
57  
58  
59  
60

1  
2  
3 distinct metals indicate that the effectiveness of the dopant depends on its chemical identity. For  
4 example, Pd is much more prone to stay on the surface than Cu, Fe, or Pt (**Figure S18**). Similarly,  
5  
6 other cations could be used, like Ca and Mg, but there is no intrinsic better stability for them,  
7  
8

9  
10 **Table S15.**

11  
12 More generally, metastable structures have shown their catalytic relevance for other materials like  
13 single atoms and cluster systems as boron nitride or nanoporous gold,<sup>70-73</sup> both from experimental  
14 and theoretical perspectives. These studies highlight the relevance of non-conventional, relatively  
15 short-live species in the overall reactivity. Our arylation catalyst thus belongs to the same family  
16  
17 of dynamic catalysts with the dominant activity being controlled by the presence of the exposed  
18  
19 Cu atoms.  
20  
21  
22  
23  
24  
25

26 Towards the design of heterogeneous catalysts for N-arylation reactions, the promoting effect  
27 evidenced here indicates that single-atom heterogeneous catalysts comprise a potential solution if  
28 the metal-host interaction can be controlled. However, the results also highlight the challenges  
29 associated with the design of stable catalysts, where in addition to commonly reported issues with  
30 leaching, the diffusion of active species into host materials also comprises a possible deactivation  
31 path. Improved experimental methods for characterizing the quantity and structure of active  
32 species and the evolution under reaction conditions will be highly valuable. However, the  
33 discrimination of metastable CuI-derived surface adsorbed species from solution phase of CuI or  
34 from Cu atoms in the bulk of GCN with existing techniques poses a major challenge and the  
35 development of new tools is beyond the scope of this manuscript.  
36  
37  
38  
39  
40  
41  
42  
43  
44  
45  
46  
47  
48  
49  
50  
51  
52  
53  
54  
55  
56  
57  
58  
59  
60

## Conclusions

In conclusion, to explore the performance in N-arylation reactions, we prepared Cu, Fe, and dual Cu-Fe single-atom heterogeneous materials based on graphitic carbon nitride via the one-pot polymerization of dicyandiamide with the corresponding metal nitrates. Although none of the single-atom materials performed well as a heterogeneous catalyst for the reaction, remarkably enhanced activity was observed upon addition of the carbon nitrides to the reference homogeneously catalyzed reaction run under optimized conditions. The largest promoting effects were evidenced upon addition of Fe<sub>1</sub>/GCN to the CuI-catalyzed reaction, achieving quantitative yields after just 4 h compared to 30% yield in the absence of a solid additive. In-depth characterization by both experimental and computational methods provided complementary insights into the reactivity of the distinct metal species anchored on carbon nitride. The inactivity of Fe and Cu atoms introduced during the synthesis of carbon nitride was related to their energetically favored stabilization in subsurface positions, preventing their participation in the reaction. In contrast, CuI adsorbed on the surface of carbon nitride during the reaction exhibited higher activity than in the purely homogeneously catalyzed reaction. Doping the lattice of carbon nitride with iron played a key role in maximizing the surface confinement of the active species, due to the lower mobility of this metal compared to copper. The promotional effect of the single-atom materials was well-described by the surface coverage of copper, which could be effectively quantified by Kinetic Monte Carlo simulations. The activation of CuI through its adsorption on the carbon nitride lattice provides a new example of the potential scope of surface confinement effects to enhance the efficiency of coupling reactions.



## AUTHOR INFORMATION

### Corresponding Author

\*msharon@chem.ethz.ch

\*nlopez@iciq.es

\*jpr@chem.ethz.ch

\*erickm.carreira@org.chem.ethz.ch

### Author Contributions

The manuscript was written through contributions of all authors. All authors have given approval to the final version of the manuscript. ‡These authors contributed equally.

### Funding Sources

Any funds used to support the research of the manuscript should be placed here (per journal style).

## ABBREVIATIONS

GCN, graphitic carbon nitride; ICP-OES, inductively coupled plasma - optical emission spectrometry; XRD, X-ray diffraction, (AC-ADF-)STEM, (aberration-corrected annular dark-field) scanning transmission electron microscopy; NND, nearest neighbor distance; EDX, energy dispersive X-ray spectroscopy; XPS, X-ray photoelectron spectroscopy; (E)XAFS, (extended) X-ray absorption fine structure; XANES, X-ray absorption near edge structure; CN, coordination number; (cw-)EPR, (continuous wave) electron paramagnetic resonance; DFT, density functional theory; KMC, kinetic Monte Carlo; DCM, dichloromethane; DMF, dimethylformamide.

## ASSOCIATED CONTENT

**Supporting Information.** Full details of the experimental protocols and complementary analytical and catalytic data are supplied as Supporting Information. This material is available free of charge via the Internet at <http://pubs.acs.org>. The computed structures are available in the ioChem-BD database under reference [reviewer link:  
<https://iochem-bd.iciq.es/browse/review-collection/100/22786/bba07174ab472a09dc553542>]

## ACKNOWLEDGMENTS

This publication was created as part of NCCR Catalysis, a National Centre of Competence in Research funded by the Swiss National Science Foundation. ScopeM at ETH Zurich is thanked for use of their facilities. V.C.G. acknowledges a fellowship of the Stipendienfonds Schweizerische Chemische Industrie (SSCI). S.M.C. acknowledges the support of a Henslow Research Fellowship at Girton College, Cambridge. P.A.M. thanks the Engineering and Physical Sciences Research Council (EPSRC) for financial support under grant number EP/R025517/1. SuperSTEM is the U.K. National Research for Advanced Electron Microscopy, supported by the EPSRC. Mr. Simon L. Rössler is acknowledged for fruitful discussions. We thank the BSC-RES for providing generous computational resources.

## REFERENCES

- (1) Ullmann, F. Ueber eine neue Bildungsweise von Diphenylaminderivaten. *Ber. Dtsch. Chem. Ges.* **1903**, *36*, 2382-2384.
- (2) Surry, D. S.; Buchwald, S. L. Biaryl Phosphane Ligands in Palladium-Catalyzed Amination. *Angew. Chem.; Int. Ed.* **2008**, *47*, 6338-6361.

- 1  
2  
3 (3) Klapars, A.; Antilla, J. C.; Huang, X.; Buchwald, S. L. A General and Efficient Copper  
4 Catalyst for the Amidation of Aryl Halides and the N-Arylation of Nitrogen Heterocycles.  
5  
6 *J. Am. Chem. Soc.* **2001**, *123*, 7727-7729.  
7  
8  
9  
10 (4) Hartwig, J. F. Evolution of a Fourth Generation Catalyst for the Amination and  
11 Thioetherification of Aryl Halides. *Acc. Chem. Res.* **2008**, *41*, 1534-1544.  
12  
13  
14 (5) Sambhagio, C.; Marsden, S. P.; Blacker, A. J.; McGowan, P. C. Copper Catalysed Ullmann  
15 Type Chemistry: From Mechanistic Aspects to Modern Development. *Chem. Soc. Rev.*  
16  
17 **2014**, *43*, 3525-3550.  
18  
19  
20  
21 (6) Shin, K.; Kim, H.; Chang, S. Transition-Metal-Catalyzed C–N Bond Forming Reactions  
22 using Organic Azides as the Nitrogen Source: A Journey for the Mild and Versatile C–H  
23  
24 Amination. *Acc. Chem. Res.* **2015**, *48*, 1040-1052.  
25  
26  
27  
28 (7) Brown, D. G.; Boström, J. Analysis of Past and Present Synthetic Methodologies on  
29 Medicinal Chemistry: Where have all the New Reactions Gone? *J. Med. Chem.* **2016**, *59*,  
30  
31 4443-4458.  
32  
33  
34  
35 (8) Ley, S. V.; Thomas, A. W. Modern Synthetic Methods for Copper-Mediated C(aryl)–O,  
36 C(aryl)–N, and C(aryl)–S Bond Formation. *Angew. Chem.; Int. Ed.* **2003**, *42*, 5400-5449.  
37  
38  
39  
40 (9) Carril, M.; SanMartin, R.; Domínguez, E. Palladium and Copper-Catalysed Arylation  
41 Reactions in the Presence of Water, with a Focus on Carbon–Heteroatom Bond Formation.  
42  
43 *Chem. Soc. Rev.* **2008**, *37*, 639-647.  
44  
45  
46  
47 (10) Correa, A.; Bolm, C. Iron-Catalyzed N-Arylation of Nitrogen Nucleophiles. *Angew. Chem.*  
48 *Int. Ed.* **2007**, *46*, 8862-8865.  
49  
50  
51 (11) Taillefer, M.; Xia, N.; Ouali, A. Efficient Iron/Copper Co-Catalyzed Arylation of Nitrogen  
52 Nucleophiles. *Angew. Chem.; Int. Ed.* **2007**, *46*, 934-936.  
53  
54  
55  
56  
57  
58  
59  
60

- 1  
2  
3 (12) Li, S.; Jia, W.; Jiao, N. Copper/Iron-Cocatalyzed Highly Selective Tandem Reactions:  
4 Efficient Approaches to  $\alpha$ - $\gamma$ -Alkylidene Lactones. *Adv. Synth. Catal.* **2009**, *351*, 569-575.  
5  
6  
7 (13) Wang, Z.; Fu, H.; Jiang, Y.; Zhao, Y. Iron/Copper-Cocatalyzed Ullmann N,O-Arylation  
8 using FeCl<sub>3</sub>, CuO, and rac-1,1'-Binaphthyl-2,2'-diol. *Synlett.* **2008**, 2540-2546.  
9  
10  
11 (14) Mao, J.; Xie, G.; Wu, M.; Guo, J.; Ji, S. Ligand-Free Iron/Copper Cocatalyzed Alkynylation  
12 Coupling Reactions. *Adv. Synth. Catal.* **2008**, *350*, 2477-2482.  
13  
14  
15 (15) Wu, X.-F.; Darcel, C. Ligand-Free Iron/Copper-Cocatalyzed Amination of Aryl Iodides.  
16  
17  
18  
19  
20  
21  
22 (16) Buchwald, S. L.; Bolm, C. On the Role of Metal Contaminants in Catalyses with FeCl<sub>3</sub>.  
23  
24  
25  
26  
27 (17) Salam, N.; Kundu, S. K.; Roy, A. S.; Mondal, P.; Roy, S.; Bhaumik, A.; Islam, S. M.  
28  
29  
30  
31  
32  
33  
34  
35  
36 (18) Kidwai, M.; Mishra, N. K.; Bhardwaj, S.; Jahan, A.; Kumar, A.; Mozumdar, S. Cu  
37  
38  
39  
40  
41  
42  
43 (19) Jadhav, V. H.; Dumbre, D. K.; Phapale, V. B.; Borate, H. B.; Wakharkar, R. D. Efficient N-  
44  
45  
46  
47  
48 (20) Kantam, M. L.; Venkanna, G. T.; Sridhar, C.; Sreedhar, B.; Choudary, B. M. An efficient  
49  
50  
51  
52  
53  
54  
55  
56  
57  
58  
59  
60

- 1  
2  
3 (21) Likhar, P. R.; Roy, S.; Roy, M.; Kantam, M. L.; De, R. L. Silica Immobilized Copper  
4  
5  
6  
7  
8  
9  
10  
11  
12  
13  
14  
15  
16  
17  
18  
19  
20  
21  
22  
23  
24  
25  
26  
27  
28  
29  
30  
31  
32  
33  
34  
35  
36  
37  
38  
39  
40  
41  
42  
43  
44  
45  
46  
47  
48  
49  
50  
51  
52  
53  
54  
55  
56  
57  
58  
59  
60
- (21) Likhar, P. R.; Roy, S.; Roy, M.; Kantam, M. L.; De, R. L. Silica Immobilized Copper Complexes: Efficient and Reusable Catalysts for N-arylation of N (H)-Heterocycles and Benzyl Amines with Aryl Halides and Arylboronic Acids. *J. Molec. Catal. A: Chem.* **2007**, *271*, 57-62.
- (22) Mitchell, S.; Vorobyeva, E.; Pérez-Ramírez, J. The Multifaceted Reactivity of Single-Atom Heterogeneous Catalysts. *Angew. Chem.; Int. Ed.* **2018**, *57*, 15316-15329.
- (23) Cui, X.; Li, W.; Ryabchuk, P.; Junge, K.; Beller, M. Bridging Homogeneous and Heterogeneous Catalysis by Heterogeneous Single-Metal-Site Catalysts. *Nat. Catal.* **2018**, *1*, 385-397.
- (24) Wang, A.; Li, J.; Zhang, T. Heterogeneous Single-Atom Catalysis. *Nat. Rev. Chem.* **2018**, *2*, 65-81.
- (25) Lang, R.; Li, T.; Matsumura, D.; Miao, S.; Ren, Y.; Cui, Y. T.; Tan, Y.; Qiao, B.; Li, L.; Wang, A.; Wang, X.; Zhang, T. Hydroformylation of Olefins by a Rhodium Single-Atom Catalyst with Activity Comparable to RhCl(PPh<sub>3</sub>)<sub>3</sub>. *Angew. Chem. Int. Ed.* **2016**, *55*, 16054-16058.
- (26) Wang, L.; Zhang, W.; Wang, S.; Gao, Z.; Luo, Z.; Wang, X.; Zeng, R.; Li, A.; Li, H.; Wang, M.; Zheng, X.; Zhu, J.; Zhang, W.; Ma, C.; Si, R.; Zeng, J. Atomic-Level Insights in Optimizing Reaction Paths for Hydroformylation Reaction over Rh/CoO Single-Atom Catalyst. *Nat. Commun.* **2016**, *7*:14036.
- (27) Chen, Z.; Vorobyeva, E.; Mitchell, S.; Fako, E.; Ortuño, M. A.; López, N.; Collins, S. M.; Midgley, P. A.; Richard, S.; Vilé, G.; Pérez-Ramírez, J. A Heterogeneous Single-Atom Palladium Catalyst Surpassing Homogeneous Systems for Suzuki Coupling. *Nat. Nanotechnol.* **2018**, *13*, 702-707.

- 1  
2  
3 (28) Zhang, L.; Wang, A.; Miller, J. T.; Liu, X.; Yang, X.; Wang, W.; Li, L.; Huang, Y.; Mou,  
4 C.-Y.; Zhang, T. Efficient and Durable Au Alloyed Pd Single-Atom Catalyst for the Ullmann  
5 Reaction of Aryl Chlorides in Water. *ACS Catal.* **2014**, *4*, 1546-1553.  
6  
7  
8  
9  
10 (29) Zhang, X.; Sun, Z.; Wang, B.; Tang, Y.; Nguyen, L.; Li, Y.; Tao, F. F. C–C Coupling on  
11 Single-Atom-Based Heterogeneous Catalyst. *J. Am. Chem. Soc.* **2018**, *140*, 954-962.  
12  
13  
14 (30) Choi, C. H.; Lee, S. Y.; Park, S. H.; Woo, S. I. Highly Active N-doped-CNTs Grafted on  
15 Fe/C Prepared by Pyrolysis of Dicyandiamide on Fe<sub>2</sub>O<sub>3</sub>/C for Electrochemical Oxygen  
16 Reduction Reaction. *Appl. Catal. B: Environ.* **2011**, *103*, 362-368.  
17  
18  
19 (31) Jing, H.; You, M.; Yi, S.; Li, T.; Ji, H.; Wang, Y.; Zhang, Z.; Zhang, R.; Chen, D.; Yang, H.  
20 Precursor-Engineering Coupled Microwave Molten-Salt Strategy Enhances Photocatalytic  
21 Hydrogen Evolution Performance of g-C<sub>3</sub>N<sub>4</sub> Nanostructures. *ChemSusChem* **2020**, *13*, 827-  
22 837.  
23  
24  
25 (32) Yonghua, D.; Zhu, Y.; Xi, S.; Yang, P.; Moser, H. O.; Breese, M. B. H.; Borgna, A. XAFCA:  
26 A New XAFS Beamline for Catalysis Research. *J. Synchrotron Radiat.* **2015**, *22*, 839-843.  
27  
28  
29 (33) Ravel, B.; Newville, M. ATHENA, ARTEMIS, HEPHAESTUS: Data Analysis for X-ray  
30 Absorption Spectroscopy using IFEFFIT. *J. Synchrotron Radiat.* **2005**, *12*, 537-541.  
31  
32  
33 (34) Newville, M. Larch: an analysis package for XAFS and related spectroscopies. *J. Phys. Conf.*  
34 *Ser.* **2013**, *430*, 012007.  
35  
36  
37 (34) Kresse, G.; Furthmüller, J. Efficient Iterative Schemes for Ab Initio Total-Energy  
38 Calculations using a Plane-Wave Basis Set. *Phys. Rev. B* **1996**, *54*, 11169.  
39  
40  
41 (35) Kresse, G.; Furthmüller, J. Efficiency of Ab-Initio Total Energy Calculations for Metals and  
42 Semiconductors using a Plane-Wave Basis Set. *Comput. Mater. Sci.* **1996**, *6*, 15-50.  
43  
44  
45  
46  
47  
48  
49  
50  
51  
52  
53  
54  
55  
56  
57  
58  
59  
60

- 1  
2  
3 (36) Perdew, J. P.; Burke, K.; Ernzerhof, M. Generalized Gradient Approximation Made Simple.  
4  
5 *Phys. Rev. Lett.* **1996**, *77*, 3865.  
6  
7  
8 (37) Grimme, S.; Antony, J.; Ehrlich, S.; Krieg, H. A Consistent and Accurate Ab Initio  
9  
10 Parametrization of Density Functional Dispersion Correction (DFT-D) for the 94 Elements  
11  
12 H-Pu. *J. Chem. Phys.* **2010**, *132*, 154104.  
13  
14  
15 (38) Blöchl, P. E. Projector Augmented-Wave Method. *Phys. Rev. B* **1994**, *50*, 17953.  
16  
17 (39) Kresse, G.; Joubert, D. From Ultrasoft Pseudopotentials to the Projector Augmented-Wave  
18  
19 Method. *Phys. Rev. B* **1999**, *59*, 1758.  
20  
21 (40) Stamatakis, M.; Vlachos, D. G. Unraveling the Complexity of Catalytic Reactions via  
22  
23 Kinetic Monte Carlo Simulation: Current Status and Frontiers. *ACS Catal.* **2012**, *2*, 2648-  
24  
25 2663.  
26  
27  
28 (41) Álvarez-Moreno, M.; de Graaf, C.; López, N.; Maseras, F.; Poblet, J. M.; Bo, C. Managing  
29  
30 the Computational Chemistry Big Data Problem: The ioChem-BD Platform. *J. Chem. Inf.*  
31  
32 *Model.* **2015**, *55*, 95-103.  
33  
34  
35 (42) Ferrando, A. R. ioChem-BD Dataset. doi: 10.19061/iochem-bd-1-151.  
36  
37  
38 (43) Vorobyeva, E.; Fako, E.; Chen, Z.; Collins, S. M.; Johnstone, D.; Midgley, P. A.; Hauert,  
39  
40 R.; Safonova, O. V.; Vilé, G.; López, N.; Mitchell, S.; Pérez-Ramírez, J. Atom-by-Atom  
41  
42 Resolution of Structure–Function Relations over Low-Nuclearity Metal Catalysts. *Angew.*  
43  
44 *Chem.; Int. Ed.* **2019**, *58*, 8724-8729.  
45  
46  
47 (44) Zang, W.; Yang, T.; Zou, H.; Xi, S.; Zhang, H.; Liu, X.; Kou, Z.; Du, Y.; Feng, Y. P.; Shen,  
48  
49 L.; Duan, L.; Wang, J.; Pennycook, S. J. Copper Single Atoms Anchored in Porous Nitrogen-  
50  
51 Doped Carbon as Efficient pH-Universal Catalysts for the Nitrogen Reduction Reaction.  
52  
53 *ACS Catal.* **2019**, *9*, 10166-10173.  
54  
55  
56  
57  
58  
59  
60

- 1  
2  
3 (45) Yang, H.; Wu, Y.; Li, G.; Lin, Q.; Hu, Q.; Zhang, Q.; Liu, J.; He, C.; Scalable Production of  
4 Efficient Single-Atom Copper Decorated Carbon Membranes for CO<sub>2</sub> Electroreduction to  
5 Methanol. *J. Am. Chem. Soc.* **2019**, *141*, 12717-12723.  
6  
7  
8  
9  
10 (46) Qu, Y.; Li, Z.; Chen, W.; Lin, Y.; Yuan, T.; Yang, Z.; Zhao, C.; Wang, J.; Zhao, C.; Wang,  
11 X. and Zhou, F. Direct Transformation of Bulk Copper into Copper Single Sites via Emitting  
12 and Trapping of Atoms. *Nat. Catal.* **2018**, *1*, 781-786.  
13  
14  
15  
16  
17 (47) Chen, Z.; Mitchell, S.; Vorobyeva, E.; Leary, R. K.; Hauert, R.; Furnival, T.; Ramasse, Q.  
18 M.; Thomas, J. M.; Midgley, P. A.; Dontsova, D.; Antonietti, M.; Pogodin, S.; López, N.;  
19 Pérez-Ramírez, J. Stabilization of Single Metal Atoms on Graphitic Carbon Nitride. *Adv.*  
20 *Funct. Mater.* **2017**, *27*, 1605785.  
21  
22  
23  
24  
25  
26 (48) Biesinger, M. C. Advanced Analysis of Copper X-ray Photoelectron Spectra. *Surf. Int. Anal.*  
27 **2017**, *49*, 1325-1334.  
28  
29  
30  
31 (49) Espinós, J. P.; Morales, J.; Barranco, A.; Caballero, A.; Holgado, J. P.; González-Elipe, A.  
32 R. Interface Effects for Cu, CuO, and Cu<sub>2</sub>O Deposited on SiO<sub>2</sub> and ZrO<sub>2</sub>. XPS Determination  
33 of the Valence State of Copper in Cu/SiO<sub>2</sub> and Cu/ZrO<sub>2</sub> Catalysts. *J. Phys. Chem. B* **2002**,  
34 *106*, 6921-6929.  
35  
36  
37  
38  
39  
40 (50) Li, J.; Pršlja, P.; Shinagawa, T.; Martín, A. J.; Krumeich, F.; Artyushkova, K.; Atanassov,  
41 P.; Zitolo, A.; Zhou, Y.; García-Muelas, R.; López, N.; Pérez-Ramírez, J.; Jaouen,  
42 F. Volcano Trend in Electrocatalytic CO<sub>2</sub> Reduction Activity over Atomically Dispersed  
43 Metal Sites on Nitrogen-Doped Carbon. *ACS Catal.* **2019**, *9*, 10426-10439.  
44  
45  
46  
47  
48  
49 (51) Daelman, N.; Capdevila-Cortada, M.; López, N. Dynamic Charge and Oxidation State of  
50 Pt/CeO<sub>2</sub> Single-Atom Catalysts. *Nat. Mat.* **2019**, *18*, 1215-1221.  
51  
52  
53  
54  
55  
56  
57  
58  
59  
60



- 1  
2  
3 (52) Biesinger, M. C.; Payne, B. P.; Grosvenor, A. P.; Lau, L. W. M.; Gerson, A. R.; Smart, R.  
4 S. C. Resolving Surface Chemical States in XPS Analysis of First Row Transition Metals,  
5 Oxides and Hydroxides: Cr, Mn, Fe, Co and Ni. *Appl. Surf. Sci.* **2011**, *257*, 2717-2730.  
6  
7  
8  
9  
10 (53) Mathies, G.; Chatziefthimiou, S. D.; Maganas, D.; Sanakis, Y.; Sottini, S.; Kyritsis, P.;  
11 Groenen, E. J. High-Frequency EPR Study of the High-Spin Fe<sup>II</sup> Complex Fe[(SPPH<sub>2</sub>)<sub>2</sub>N]<sub>2</sub>.  
12 *J. Magn. Resonance* **2012**, *224*, 94-100.  
13  
14  
15  
16  
17 (54) Dong, L.; Liu, P. N.; Lin, N. Surface-Activated Coupling Reactions Confined on a Surface.  
18 *Acc. Chem. Res.* **2015**, *48*, 2765-2774.  
19  
20  
21 (55) Antilla, J. C.; Baskin, J. M.; Barder, T. E.; Buchwald, S. L. Copper–Diamine-Catalyzed  
22 N-Arylation of Pyrroles, Pyrazoles, Indazoles, Imidazoles, and Triazoles. *J. Org. Chem.*  
23 **2004**, *69*, 5578-5587.  
24  
25  
26  
27  
28 (56) Sherborne, G. J.; Adomeit, S.; Menzel, R.; Rabeah, J.; Brückner, A.; Fielding, M. R.;  
29 Willans, C. E.; Nguyen, B. N. Origins of High Catalyst Loading in Copper (I)-Catalysed  
30 Ullmann–Goldberg C–N Coupling Reactions. *Chem. Sci.* **2017**, *8*, 7203-7210.  
31  
32  
33  
34  
35 (57) Batsanov, A. S.; Hubberstey, P.; Russell, C. E. Intramolecular Hydrogen-bonding  
36 Stabilisation of Tetrafluoroborate Co-ordination to Copper(II): Crystal Structure of  
37 (2,2'-Bipyridine)bis(2-cyanoguanidine)bis-(tetrafluoroborato)copper(II). *J. Chem. Soc.*  
38 *Dalton Trans.* **1994**, 3189-3190.  
39  
40  
41  
42  
43  
44 (58) Sperotto, E.; van Klink, G. P.; van Koten, G.; de Vries, J. G. The Mechanism of the Modified  
45 Ullmann Reaction. *Dalton Trans.* **2010**, *39*, 10338-10351.  
46  
47  
48  
49 (59) Jones, G. O.; Liu, P.; Houk, K.; Buchwald, S. L. Computational Explorations of Mechanisms  
50 and Ligand-Directed Selectivities of Copper-Catalyzed Ullmann-Type Reactions. *J. Am.*  
51 *Chem. Soc.* **2010**, *132*, 6205-6213.  
52  
53  
54  
55  
56  
57  
58  
59  
60

- 1  
2  
3 (60) Yu, H.-Z.; Jiang, Y.-Y.; Fu, Y.; Liu, L. Alternative Mechanistic Explanation for Ligand-  
4 Dependent Selectivities in Copper-Catalyzed N-and O-Arylation Reactions. *J. Am. Chem.*  
5 *Soc.* **2010**, *132*, 18078-18091.  
6  
7  
8  
9  
10 (61) Larsson, P. F.; Wallentin, C. J.; Norrby, P. O. Mechanistic Aspects of Submol %  
11 Copper-Catalyzed C – N Cross-Coupling. *ChemCatChem* **2014**, *6*, 1277-1282.  
12  
13  
14 (62) Gutsev, G. L.; Mochena, M. D.; Jena, P.; Bauschlicher, C. W.; Partridge, H. Periodic Table  
15 of 3d-Metal Dimers and their Ions. *J. Chem. Phys.* **2004**, *121*, 6785-6797.  
16  
17  
18  
19 (63) Strieter, E. R.; Bhayana, B.; Buchwald, S. L. Mechanistic Studies on the Copper-Catalyzed  
20 N-Arylation of Amides. *J. Am. Chem. Soc.* **2009**, *131*, 78-88.  
21  
22  
23  
24 (64) Strieter, E. R.; Blackmond, D. G.; Buchwald, S. L. The Role of Chelating Diamine Ligands  
25 in the Goldberg Reaction: A Kinetic Study on the Copper-Catalyzed Amidation of Aryl  
26 Iodides. *J. Am. Chem. Soc.* **2005**, *127*, 4120-4121.  
27  
28  
29  
30  
31 (65) Ouali, A.; Taillefer, M.; Spindler, J. F.; Jutand, A. Precatalysts Involved in Copper-  
32 Catalyzed Arylations of Nucleophiles. *Organometallics*, *26*, 65-74.  
33  
34  
35 (66) Ouali, A.; Spindler, J. F.; Jutand, A.; Taillefer, M. Nitrogen Ligands in Copper-Catalyzed  
36 Arylation of Phenols: Structure/Activity Relationships and Applications. *Adv. Syn. Catal.*  
37 **2007**, *349*, 1906-1916.  
38  
39  
40  
41  
42 (67) Kiyomori, A.; Marcoux, J. F.; Buchwald, S. L. An Efficient Copper-Catalyzed Coupling of  
43 Aryl Halides with Imidazoles. *Tetrahedron Lett.* **1999**, *40*, 2657-2660.  
44  
45  
46  
47 (68) Gujadhur, R. K.; Bates, C. G.; Venkataraman, D. Formation of Aryl–Nitrogen,  
48 Aryl–Oxygen, and Aryl–Carbon Bonds using well-defined Copper (I)-based Catalysts. *Org.*  
49 *Lett.* **2001**, *3*, 4315-4317.  
50  
51  
52  
53  
54  
55  
56  
57  
58  
59  
60

- 1  
2  
3 (69) Monnier, F.; Taillefer, M. Catalytic C–C, C–N, and C–O Ullmann-Type Coupling  
4  
5 Reactions. *Angew. Chem. Int. Ed.* **2009**, *48*, 6954-6971.  
6  
7  
8 (70) Zhang, Z.; Jimenez-Izal, E.; Hermans, I.; Alexandrova, A. N. Dynamic *Phase* Diagram of  
9  
10 Catalytic Surface of Hexagonal Boron Nitride under Conditions of Oxidative  
11  
12 Dehydrogenation of Propane. *J. Phys. Chem. Lett.* **2019**, *10*, 1, 20-25.  
13  
14  
15 (71) Biener, J.; Biener, M. M.; Madix, R. J.; Friend, C. M. Nanoporous Gold – Understanding  
16  
17 the Origin of the Reactivity of a 21<sup>st</sup> Century Catalyst Made by Pre-Columbian Technology.  
18  
19 *ACS Catal.* **2015**, *5*, 6263-6270.  
20  
21  
22 (72) Zhang, Z.; Zandkarimi, B.; Alexandrova, A. N. Ensembles of Metastable States Govern  
23  
24 Heterogeneous Catalysis on Dynamic Interfaces. *Acc. Chem. Res.* **2020**, *53*, 447-458.  
25  
26  
27 (73) Peters, B.; Scott, S. L. Single Atom Catalysts on Amorphous Supports: A Quenched Disorder  
28  
29 Perspective. *J. Chem. Phys.* **2015**, *142*, 104708.  
30  
31  
32  
33  
34  
35  
36  
37  
38  
39  
40  
41  
42  
43  
44  
45  
46  
47  
48  
49  
50  
51  
52  
53  
54  
55  
56  
57  
58  
59  
60

**Tables and Figures****Table 1.** Metal Contents of the As-Synthesized SAHCs and of Fe<sub>1</sub>/GCN after Reuse in Consecutive Catalytic Runs.

Sample	State	Fe / wt%		Cu / wt%	
		Bulk <sup>a</sup>	Surface <sup>b</sup>	Bulk <sup>a</sup>	Surface <sup>b</sup>
Cu <sub>1</sub> /GCN	Fresh	0.00	0.00	1.70	0.02
Fe <sub>1</sub> /GCN	Fresh	4.06	0.03	0.00	0.00
	Run 1 <sup>c</sup>	4.10	0.01	0.23	0.05
	Run 3 <sup>c</sup>	4.04	0.00	0.62	0.12
	Run 5 <sup>c</sup>	4.03	0.00	0.40	0.08
Cu <sub>1</sub> Fe <sub>1</sub> /GCN	Fresh	2.17	0.01	4.29	0.02

<sup>a</sup> ICP-OES, <sup>b</sup> XPS, <sup>c</sup> Recovered after use in the reactions described in **Figure 5**.

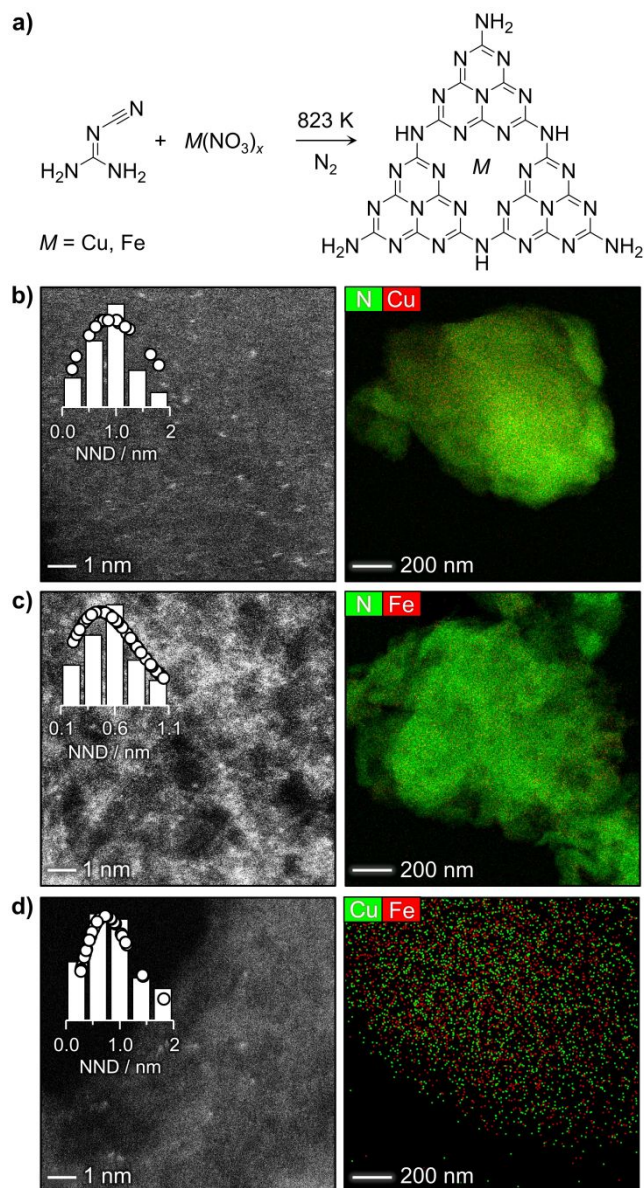


**Figure 1.** a) Approach to synthesize Cu- and Fe-containing SAHCs. AC-ADF-STEM images and elemental maps at lower magnification of b)  $\text{Cu}_1/\text{GCN}$ , c)  $\text{Fe}_1/\text{GCN}$  and d)  $\text{Cu}_1\text{Fe}_1/\text{GCN}$ . Nearest neighbor distance (NND) distributions (bars) with corresponding pair distribution function (circles) are shown inset. Additional AC-ADF-STEM images are provided in **Figure S2**. EDX spectra corresponding to the elemental maps are presented in **Figure S3**.

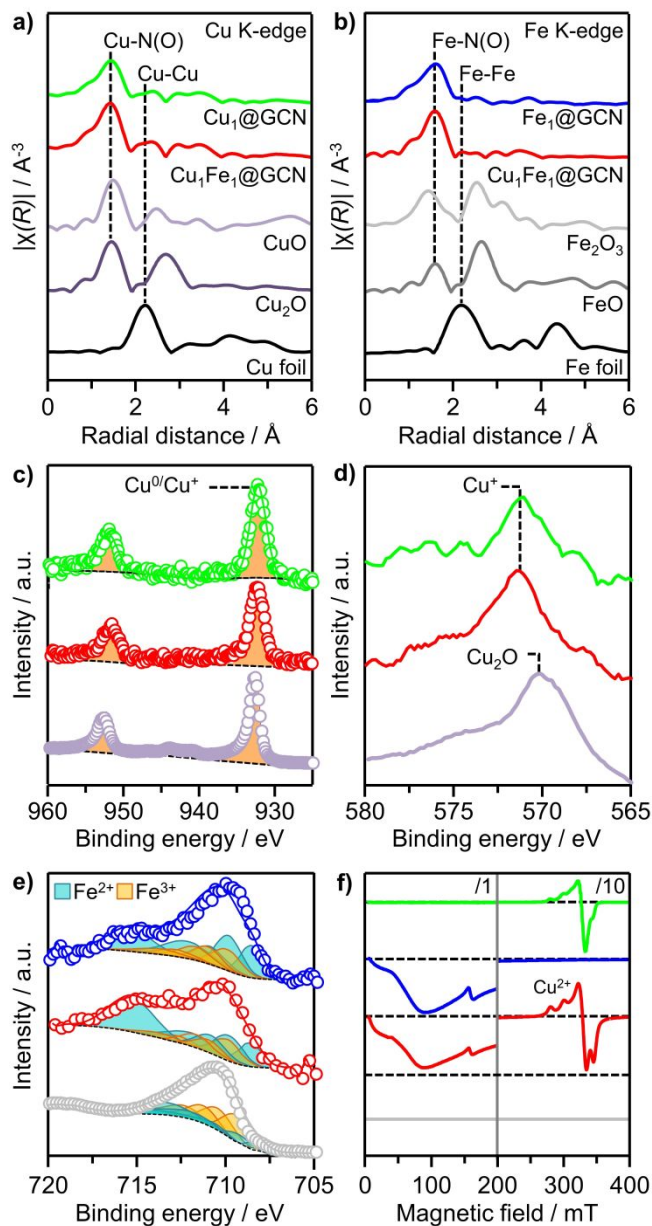


**Figure 2.** a) Cu K-edge and b) Fe K-edge Fourier transformed EXAFS spectra, c) Cu 2p XPS, d) Auger, e) Fe 2p XPS, and f) Cw-EPR spectra of the Cu- and Fe-containing SAHCs and reference compounds. The sample color codes in (a,b) apply to (c-f). The full assignment of the fits in (d) is provided in **Figure S7**.

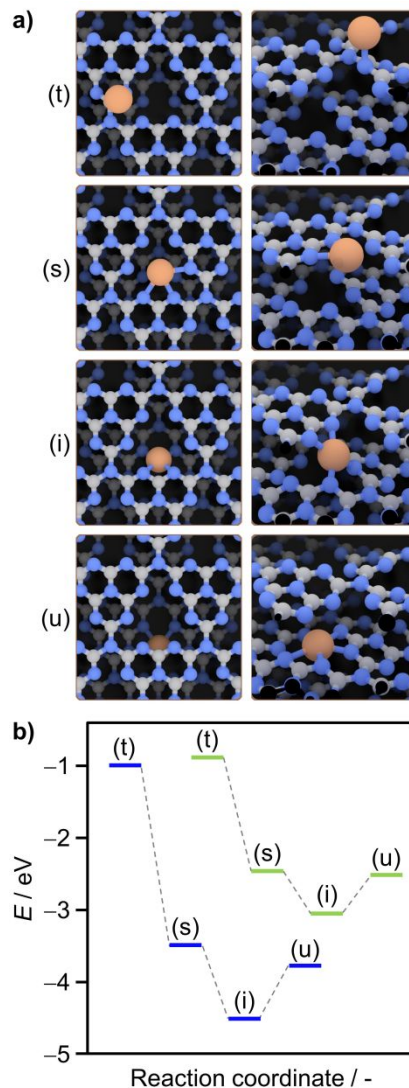


**Figure 3.** a) Modeled supercell showing top (t), surface heptazinic (s), interlayer (i), and under-the-surface heptazinic (u) coordination sites for Cu (green) or Fe (blue) atoms in top (left) or side (right) view. b) Corresponding formation energies of the sites with reference to an empty cavity and isolated atom. Color code: C-gray; N-blue; Fe-orange; I-purple; H-white.

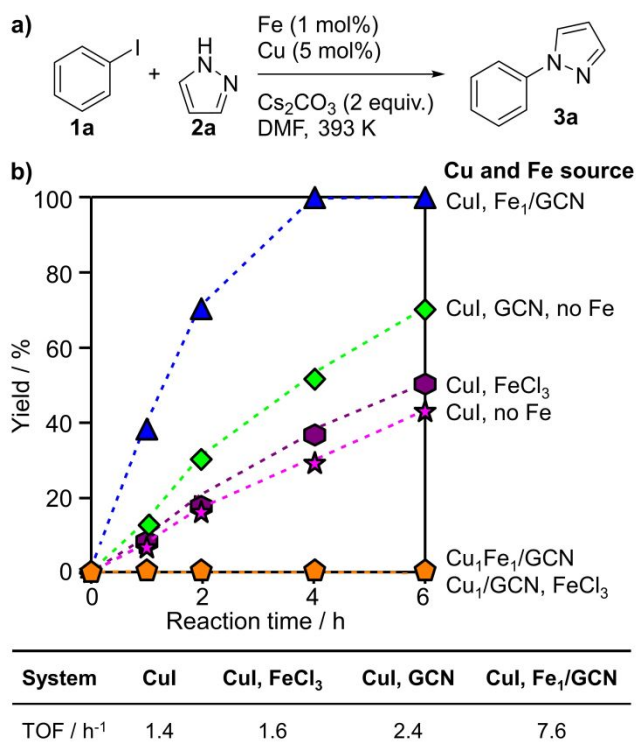


**Figure 4.** a) N-arylation of pyrazole with iodobenzene and reaction conditions. b) Yield of 1-phenylpyrazole (**3a**) as a function of the reaction time with varying Cu and Fe sources. The table indicates the initial turnover frequency (TOF) determined after 1 h based on the Cu content. Reactions were conducted on a 0.3 mmol scale. Yields were determined by GC analysis of the unpurified reaction mixture and were averaged over two runs.



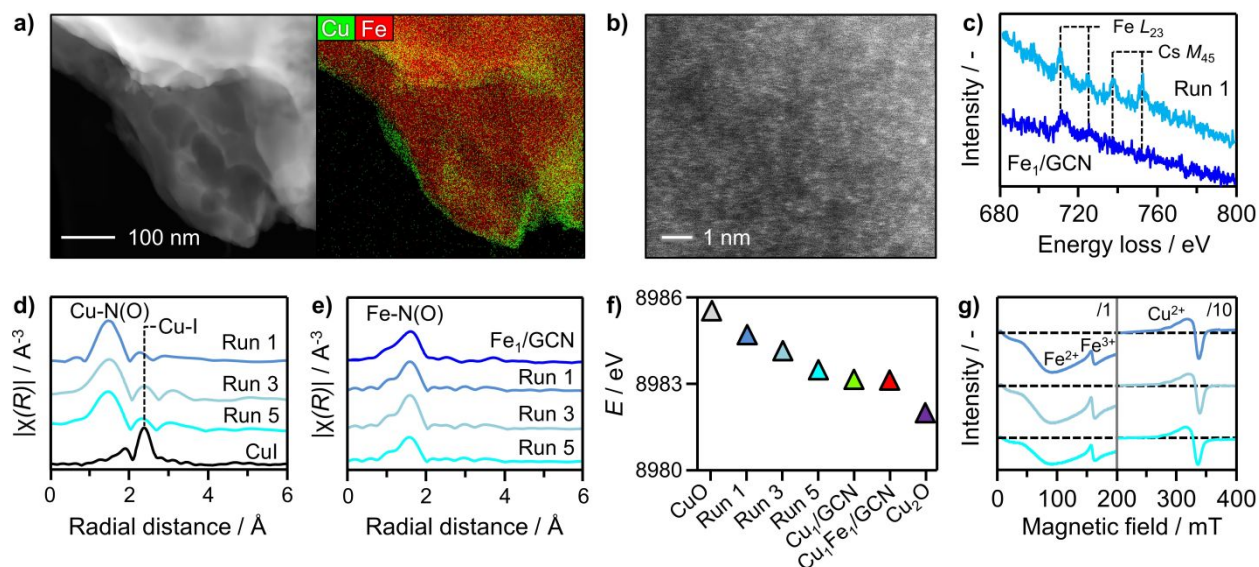
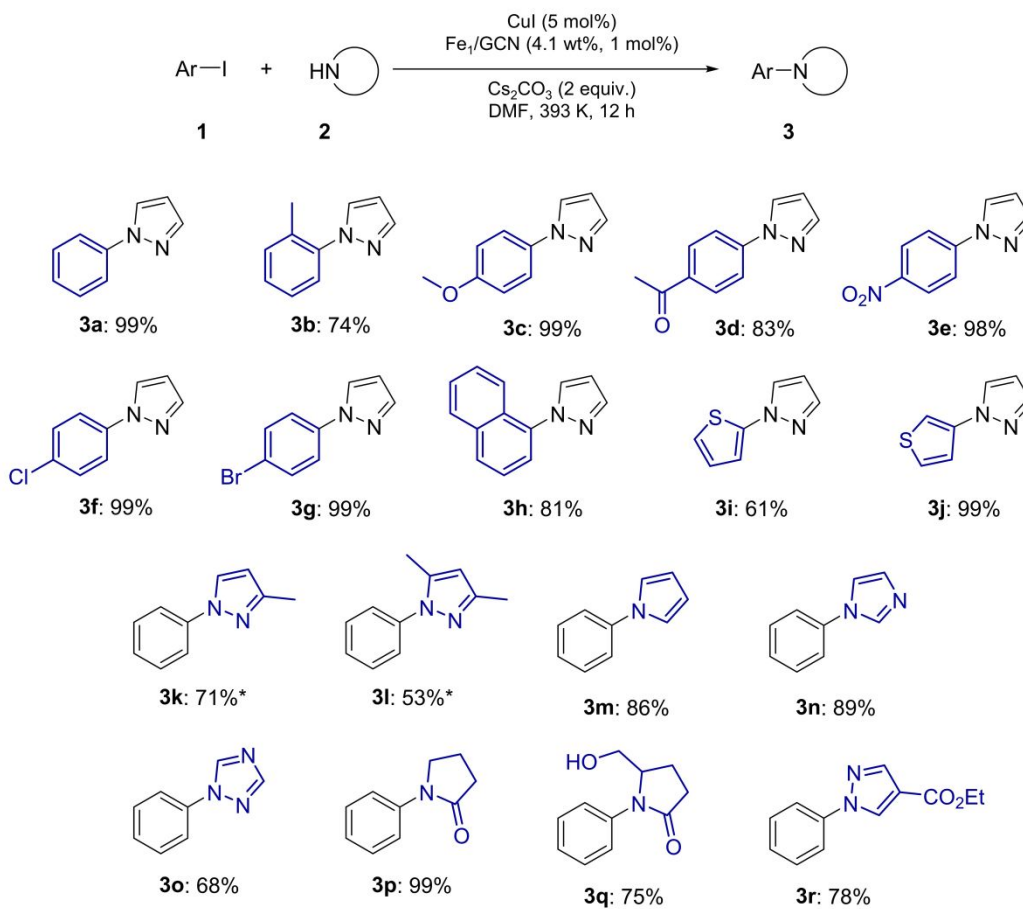


**Figure 5.** a) HAADF-STEM image and corresponding elemental map, b) AC-ADF-STEM image, and c) EELS spectra of  $\text{Fe}_1/\text{GCN}$  after use in consecutive runs of the N-arylation of pyrazole. d) Cu and e) Fe K-edge FT-EXAFS spectra, f) the position of the Cu K-edge derived from the XANES spectra presented in **Figure S4**, and g) Cw-EPR spectra of  $\text{Fe}_1/\text{GCN}$  after use in consecutive catalytic runs. Reaction conditions as described in **Figure 3** with  $t = 12$  h.



33 **Figure 6.** Scope of the Fe<sub>1</sub>/GCN promoted *N*-arylation. Reactions were conducted on 0.3 mmol  
 34 scale. Yields refer to the isolated product after purification. \*Reactions were run for 48 h.  
 35  
 36  
 37  
 38  
 39  
 40  
 41  
 42  
 43  
 44  
 45  
 46  
 47  
 48  
 49  
 50  
 51  
 52  
 53  
 54  
 55  
 56  
 57  
 58  
 59  
 60

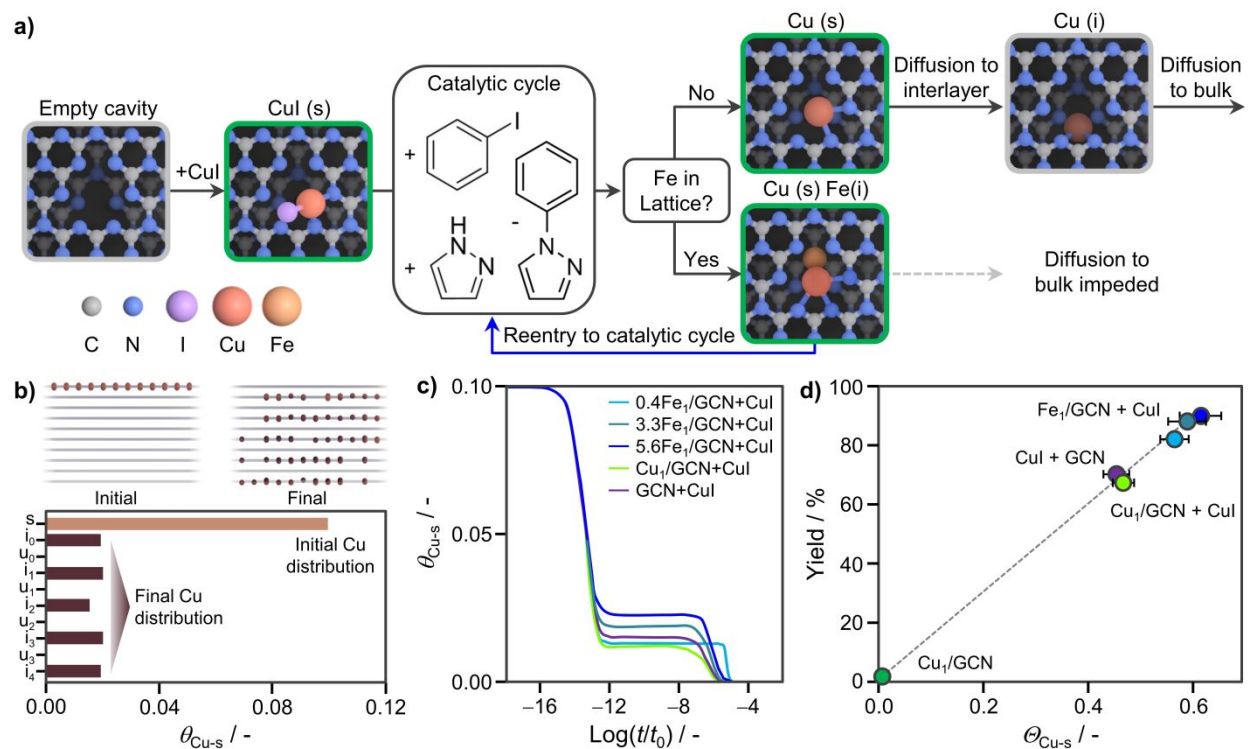


**Figure 7.** a) Potential route for the activation of CuI via coordination with the GCN surface, permitting the initiation of a surface-confined catalytic cycle. Green boxes highlight copper species that can catalyze N-arylation. After the reaction, a single Cu atom remaining in the surface cavity has a high probability to deactivate by diffusion into the bulk of the host (black arrows) due to the increased stability of interlayer positions. In Fe<sub>1</sub>/GCN, the presence of Fe occupying interlayer positions prevent percolation of Cu atoms, confining them to the surface and enabling their reintroduction into the catalytic cycle (blue arrow). b) Initial and final configurations of a KMC run where Cu atoms originally present in surface “s” sites converge to a homogeneous distribution in all available interlayer positions “i”. c) Cu population on surfaces of different carriers as a function of time denoted as  $\theta_{Cu-s}(t)$ . d) Correlation between experimental yield of arylation with Fe<sub>1</sub>/GCN, Cu<sub>1</sub>/GCN and GCN carriers as a function of their capacity for retaining Cu on the surface  $\theta$ , as defined in **Equation S2**. The linear fitting obtained was  $\text{Yield} = 0 \pm 3 + (149 \pm 7) \theta$  with a correlation coefficient  $r^2 = 0.98$ . Color code: Cu-red; N-blue; C-gray; I-purple.

## Table of Contents Graphic

